Wind load effects on photovoltaic modules

Juan M. Podesta[1], Javier L. Mroginski[1], Hugo G. Castro[1], Adrián R. Wittwer[2]

[1]*Computational Mechanics Laboratory (LAMEC-IMIT-CONICET), Northeast National University (UNNE)*
Av. Las Heras 727, H3500COI, Chaco, Argentina
jmapodesta@gmail.com, javiermro@gmail.com, castrohgui@gmail.com
[2]*Aerodynamics Laboratory, Engineering Faculty, Northeast National University (UNNE)*
Av. Las Heras 727, H3500COI, Chaco, Argentina
arwittwer@gmail.com

Abstract. Wind loads are a major concern regarding steel structures, which is the case of the photovoltaic modules. These devices have been studied using different approaches in order to determine their aerodynamic characteristics. Nevertheless, the argentine regulation in this aspect (CIRSOC 102 Ed. 2005) does not contribute with detailed specifications for unconventional structures. In order to provide more data about the influence of the photovoltaic module aerodynamics on its constitutive structural elements, an interdisciplinary approach is presented to define the aerodynamic properties and the mechanical states of a specific model of the photovoltaic module. In the first place, the pressure coefficients obtained experimentally in the Wind Tunnel by other authors were used to determine the most hostile wind loads applied to the studied panel. Secondly, numerical modeling of the type structure in the physical and geometric nonlinear field was carried out, thus obtaining the natural modes of vibration and the structural components with critical solicitation.

Keywords: Wind loads, Photovoltaic modules, Finit element method

1 Introduction

It is well known that in order to represent wind loads adequately by wind tunnel testing, similitude laws, and scaling relationships must be applied. In the case of solar panels, several characteristics must be taken into account like wind speed, terrain characteristics, the geometry of the panels, among other factors [1]. Besides, computational fluid dynamics (CFD) offers another insight into the determination of wind forces on structures. Furthermore, by using CFD is possible to visualize and quantify unsteady vortex structures, enhancing understanding of the complex dynamics of coherent structures in turbulent flows. This work presents CFD computations of ground-mounted solar panels, considering different geometries, wind directions, and wind speeds. Also, a numerical study is carried out, where wind loads obtained by wind tunnel tests are applied to the solar panel geometry, to determine critical sections of the structure.

2 Computational Fluid Dynamics

2.1 Geometry modeling

Different solar panel geometries are considered in this research. The complete arrangement of solar panels can be seen in Fig.(1) with approximately 36 meters long (configuration 1, *C1*). Another geometrical configuration (configuration 2, *C2*, approximately 6 meters long) is shown in Fig.(2). The wind direction angle reference (ϕ) is also shown in Fig.(2 *b*). Inclination angle α is indicated in Fig.(2) which can take values of $0°$ and $20°$, and is valid for both configurations.
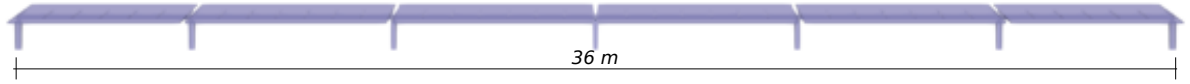
Figure 1. Full solar panel array (36m long) - Front view.
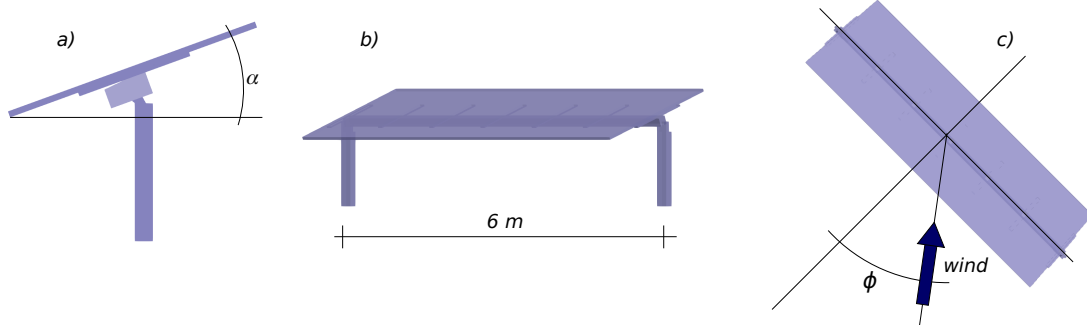
Figure 2. a) Lateral view. b) Perspective view. c) Upper view. Isolated solar panel array (6m long).

2.2 Boundary conditions

The lateral and top walls of the computational domain are considered as slip walls, while the solar panel and the floor plane are treated as no-slip walls, see Fig.(3). At the domain's inlet, a wind velocity profile is imposed. This profile is representative of an atmospheric boundary layer, using the power-law equation:

$$\frac{u(z)}{U_{ref}} = \left(\frac{z}{z_g}\right)^{\beta} \tag{1}$$

where z_g is the atmospheric boundary layer height of the terrain, U_{ref} is the mean wind velocity, β is a coefficient that depends on the terrain roughness and z is the distance from the ground. In this study, the near-field environment is classified as "open terrain", with $\beta = 0.16$ and $z_g = 10$m.
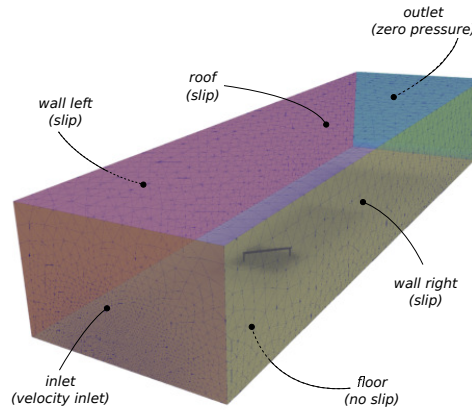
Figure 3. Boundary conditions on the computational domain.

To introduce a realistic unsteady inflow, a synthesized wind velocity field is applied on the inlet plane. A method known as modified discretizing and synthesizing random flow generation (MDSRFG) [2, 3] is used here to represent the statistical characteristics of the turbulence. The parameters to be defined are,

$$u_i(x,t) = \sum_{m=1}^{M} \sum_{n=1}^{N} p_i^{m,n} \cos(\tilde{k}_j^{m,n} \tilde{x}_j + \omega_{m,n} \frac{t}{\tau_0}) + q_i^{m,n} \sin(\tilde{k}_j^{m,n} \tilde{x}_j + \omega_{m,n} \frac{t}{\tau_0}), \tag{2}$$

and

$$p_i^{m,n} = sign(r_i^{m,n}) \sqrt{\frac{2}{N} S_i(f_m) \Delta f \frac{(r_i^{m,n})^2}{1+(r_i^{m,n})^2}}, \quad q_i^{m,n} = sign(r_i^{m,n}) \sqrt{\frac{2}{N} S_i(f_m) \Delta f \frac{1}{1+(r_i^{m,n})^2}}, \tag{3}$$

where τ_0 is a dimensionless parameter to allow control over time correlation of the velocity fluctuations and Δf is the frequency bandwidth defined by the spectra discretization. About the turbulence modeling, all CFD simulations are implemented using the Large Eddy Simulation method (LES). The LES model solves the filtered Navier-Stokes equations [4].

2.3 Unsteady results

Time histories of lift and drag coefficients are shown in Fig.(4) for configuration 2. These coefficients are defined as:

$$C_L = \frac{F_L}{0.5 \, \rho \, U_{ref}^2} \qquad C_D = \frac{F_D}{0.5 \, \rho \, U_{ref}^2} \qquad (4)$$

where F_L is the lift force, F_D is the drag force and ρ is the air density (1.225 kg/m^3).
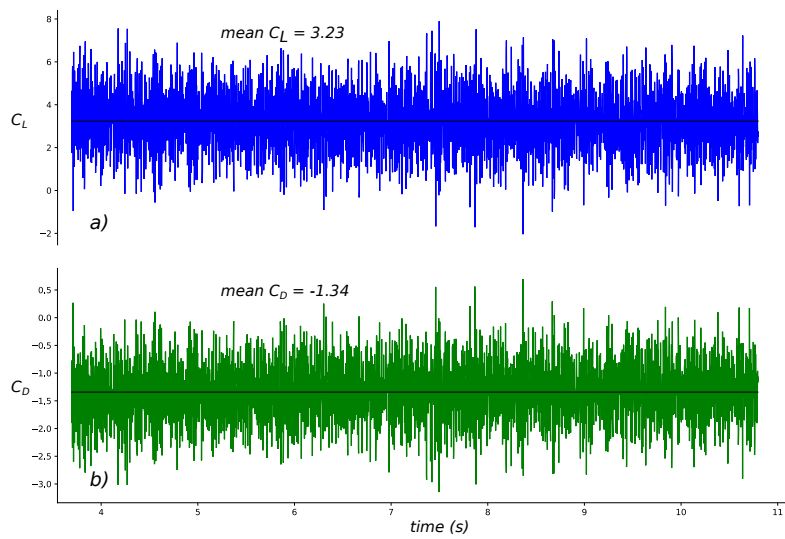
Figure 4. Unsteady forces over $C2$ (25 m/s, $\alpha = 20°$, $\phi = 0°$).

2.4 Flow structures

Both forces and pressures on the structure provide quantitative information about the aerodynamics of the solar panel structure. Nevertheless, in order to describe more efficiently the unsteady phenomena taking place in the flow field, it is necessary to examine the instantaneous vorticity. To obtain a three-dimensional analysis of the instantaneous flow structures, in this work the Q-criterion is used. This parameter is defined as the second invariant of the velocity gradient tensor [5]:

$$Q = \frac{1}{2}(\Omega_{ij}\Omega_{ij} - S_{ij}S_{ij}), \qquad (5)$$

where S_{ij} is the rate-of-strain tensor and Ω_{ij} is the rate-of-rotation tensor which being the symmetric and antisymmetric parts of the velocity gradient tensor $A_{ij} = \partial u_i / \partial x_j$ respectively, i.e.,

$$S_{ij} = (A_{ij} + A_{ji})/2 \qquad \text{and} \qquad \Omega_{ij} = (A_{ij} - A_{ji})/2. \qquad (6)$$

The physical interpretation of equation (5) is that the second invariant Q is a balance between the strain rate S_{ij} and the rotation rate Ω_{ij} which implies that positive Q isosurfaces exhibit zones where the amount of rotation exceeds the strain. It is possible to observe that the vortices follow the pressure distribution obtained by the wind tunnel tests. In all cases, streamwise vortices form in the wake, stretching and expanding with increasing downstream distance.
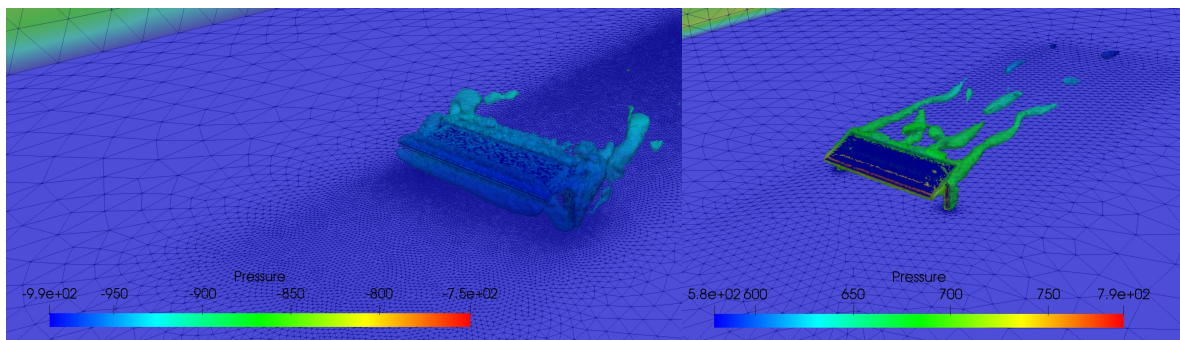
Figure 5. Instantaneous Q isosurfaces - *C2*. *Left:* $\alpha = 0$, $\phi = 0$, wind speed: 40 m/s. *Right:* $\alpha = 20$, $\phi = 0$, wind speed: 25 m/s.

3 Numerical analysis of the solid continua

3.1 Domain discretization

The adopted discretization is presented in Fig.(6). The finite element adopted for the full 3D simulation was the well known isoparametric 8-node Hetrahedral FE with 8 quadrature integration points (full integration). The adopted FE is very appropriated for constitutive modeling of solid continua regarding linear and non-linear analysis, which is the main aim of this work.
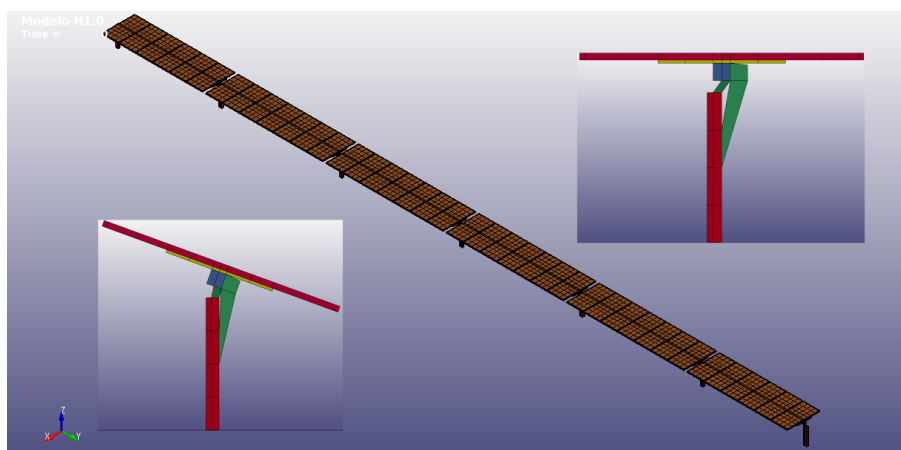
Figure 6. Finite element discretization of the full array. It can be seen two positions of the solar cells, $0°$ and $20°$ as well as an isometric perspective.

3.2 Natural frequency

Table 1. Natural frequency for the six tracks array. Columns **a**: slope at $0°$. Columns **b**: slope at $20°$

MODE	EIGENVALUE[a]	RADIANS[a]	CYCLES[a]	EIGENVALUE[b]	RADIANS[b]	CYCLES[b]
1	7.990482E+02	2.826744E+01	4.498903E+00	8.260982E+02	2.874192E+01	4.574419E+00
2	7.997929E+02	2.828061E+01	4.500999E+00	8.263409E+02	2.874615E+01	4.575091E+00
3	8.522724E+02	2.919370E+01	4.646322E+00	8.603106E+02	2.933105E+01	4.668182E+00
4	8.843771E+02	2.973848E+01	4.733026E+00	8.792213E+02	2.965167E+01	4.719209E+00
5	9.968771E+02	3.157336E+01	5.025056E+00	1.040985E+03	3.226430E+01	5.135022E+00

The problem known as spectral analysis can be solved by obtaining the solution of the following equation (see [7–9]):

$$\det\left(K_{ij} - M_{ij}\omega_I^2\right) = 0 \qquad (7)$$

The numerical study performed in this work is restricted to the first 20 natural frequencies and deformation patterns. Table 1 presents the results of the first five spectral analysis performed on the solar panel. In figure (7), it is presented the first four vibration modes of the initial configuration for 0° slope.
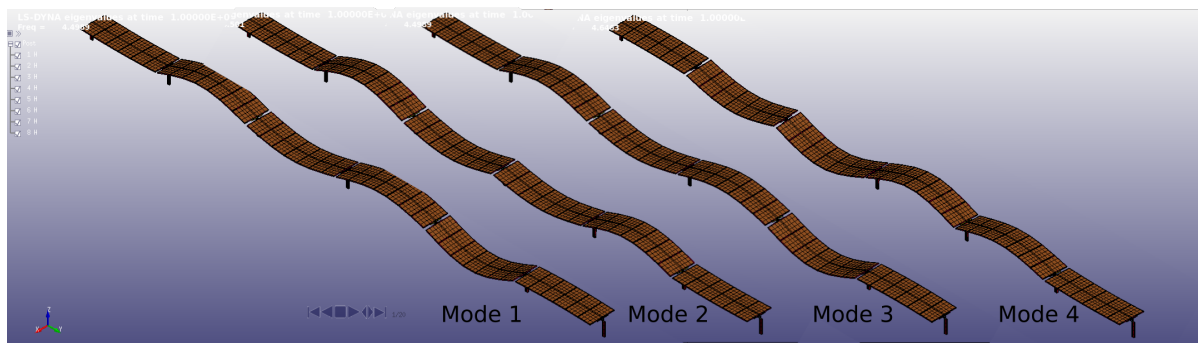
Figure 7. Natural frequencies 1 to 4

3.3 Stress determination - External Forces

The experimental results obtained by the wind tunnel tests are applied as external forces on the surfaces of the solar panels. The transformation of the dimensionless pressure coefficient, C_p, to real pressures corresponding to a prescribed value of the wind velocity $U\ [m/s]$ is obtained with the following expression:

$$p = \frac{1}{2}\,\rho\,C_p\,U^2 \qquad [Pa] = \frac{1}{2}\,[kg/m^3]\,C_p\,[m/s]^2 \tag{8}$$

being $\rho\ [kg/m^3]$ the air density. Then, in order to get the external force applied over each pressure measurement point, the above value of p obtained with Eq.(8) should be multiplied by each influence region, $A_p[m^2]$, and the resulting force will be expressed in $F[N]$.

$$F[N] = p[Pa]A_p[m^2] \tag{9}$$

In Fig.(8) the difference between the dimensionless pressure coefficient registered under and above the panel (net dimensionless pressure coefficient) is presented.
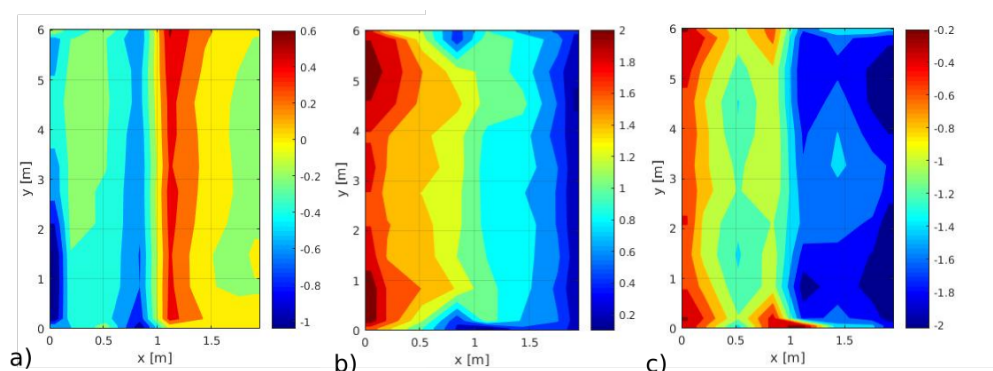
Figure 8. Net dimensionless pressure coefficient for: a) wind direction: 0°, panel slope: 0°; b) wind direction: 0°, panel slope: 20°; c) wind direction: 180°, panel slope: 20°

3.4 Stress determination - Static analysis

Due to the geometrical complexity of the full model, the stress-strain analysis is performed by considering each structure element individually. Those solid elements are identified in Fig. (9). In table 2, the main results are summarized. The critical value of each stress indicator is reported in bold style.
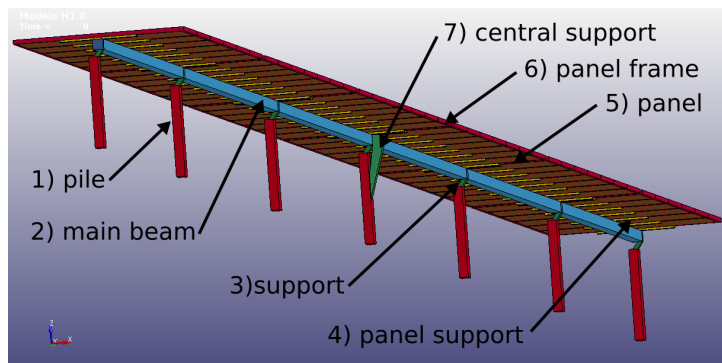
Figure 9. Structural elements identification

Table 2. Static analysis. Columns a: 0° panel slope and $U = 40m/s$; Columns b: 20° panel slope, 180° of wind direction and $U = 25m/s$

ELEMENT	I1 [a]	J2[a]	Von Mises stress[a]	I1[b]	J2[b]	Von Mises stress[b]
Pile	**3.7E+6**	**7.7E+6**	3.6E+6	3.9E+6	1.6E+6	5.2E+6
Main beam	1.2E+6	9.8E+4	1.6E+6	2.9E+6	2.9E+5	3.3E+6
Support	7.7E+5	2.0E+4	4.5E+5	3.2E+6	4.6E+5	2.8E+6
Panel support	3.0E+6	1.4E+6	**5.6E+6**	**4.1E+6**	**2.4E+6**	8.3E+6
Panel	3.0E+5	7.7E+4	5.6E+5	4.5E+5	9.7E+4	**8.6E+5**
Panel frame	1.2E+6	4.6E+5	2.9E+6	8.5E+5	6.9E+5	3.4E+6
Central support	1.4E+6	1.8E+5	1.8E+6	1.9E+6	1.1E+5	2.6E+6

3.5 Detailed study of the horizontal case

Special attention has been paid on the horizontal case (0° slope) in order to perform a detailed analysis of the real situation of the full tracker array studied in the previous sections. In contrast to the above analysis, the domain discretization for the finite element analysis of each structural elements considers its real geometry (see Figure 10). Also, in order to get the appropriate effort (or stretching) of the central support device, a beam element was included.
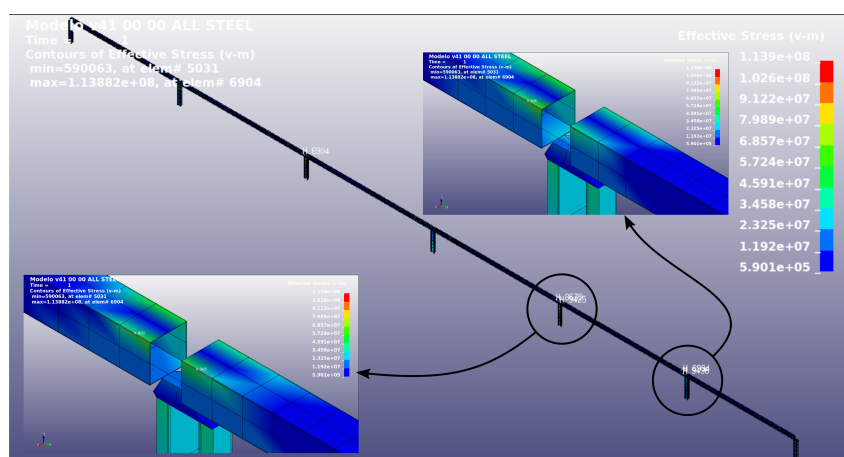
Figure 10. Von Mises stress distribution on critical sections

Figure 10 shows that there are no sections on the entire structure that exceeds the elastic limit (assuming Steel F240, $\sigma_f \approx 240$ MPa $= 2.4E + 08$ Pa). These numerical results are consistent with those obtained in the previous section. Additionally, the total effort reported with the central beam element is summarized in Table 3. Although Table 3 presents numerical results for different wind speed, it should be mentioned that the last column (60m/s) is out the aerodynamic hypothesis assumed in this report.

Table 3. Total effort of central beam support

Wind speed [m/s]	25	40	50	60
Total force [N]	-2.723E+03	-6.977E+03	-10.89E+03	-15.67E+03

There are no technical specifications (accurate geometry, material properties, etc.) of the central support device. So the efforts provided on Table 3 cannot be used to establish the security degree of the structural element. However, it can be used as a good approximation of the resultant force required to be absorbed by the structural element.

3.6 Conclusions

Regarding the spectral analysis of the full array, it can be concluded that the natural frequency of the panels is almost independent of the slope angle. These natural frequencies should be compared against the wind frequency in order to avoid any probability of resonance phenomena.

Although there are many critical sections identified during this work, none of them exceeds the elastic limits and therefore stays within the security side. However, the panel support located in the middle of the main beam as well as the central support device which join the main beam of the left with the one on the right, are the most critical structure components. On the other hand, in order the get a more accurate response about the real failure process additional studies should be performed, for example, fatigue analysis, non-linear constitutive modeling, buckling, among others.

The full development of the present research can be seen in [10].

Authorship statement. The authors hereby confirm that they are the sole liable persons responsible for the authorship of this work, and that all material that has been herein included as part of the present paper is either the property (and authorship) of the authors, or has the permission of the owners to be included here.

References

[1] A. M. Aly. On the evaluation of wind loads on solar panels: The scale issue. *Solar Energy*, vol. 135, pp. 423 – 434, 2016.

[2] H. Castro and R. Paz. A time and space correlated turbulence synthesis method for large eddy simulations. *Journal of Computational Physics*, vol. 235, pp. 742–763, 2013.

[3] H. G. Castro, R. R. Paz, J. L. Mroginski, and M. A. Storti. Evaluation of the proper coherence representation in random flow generation based methods. *Journal of Wind Engineering and Industrial Aerodynamics*, vol. 168, pp. 211 – 227, 2017.

[4] P. Sagaut. *Large Eddy Simulation for Incompressible Flows. An Introduction*, volume Third Edition of *Scientific computation*. Springer-Verlag Berlin Heidelberg, 2006.

[5] J. Hunt, A. Wray, and P. Moin. Eddies, stream and convergence zones in turbulent flows. In *Center of Turbulence Research Report*, pp. 193–208, 1998.

[6] J. L. Mroginski and G. Etse. Discontinuous bifurcation analysis of thermodynamically consistent gradient poroplastic materials. *International Journal of Solids and Structures*, vol. 51(9), pp. 1834–1846, 2014.

[7] G. B. Warburton. Structural dynamics - an introduction to computer methods. *Journal of Sound and Vibration*, vol. 84 (4), pp. 611 – 612, 1982.

[8] A. Sofi, G. Muscolino, and I. Elishakoff. Natural frequencies of structures with interval parameters. *Journal of Sound and Vibration*, vol. 347, pp. 79–95, 2015.

[9] N. K. Vaja, O. R. Barry, and E. Y. Tanbour. On the modeling and analysis of a vibration absorber for overhead powerlines with multiple resonant frequencies. *Engineering Structures*, vol. 175, pp. 711 – 720, 2018.

[10] A. R. Wittwer, J. M. Podestá, H. G. Castro, J. L. Mroginski, J. O. Marighetti, M. E. De Bortoli, R. R. Paz, and F. Mateo. Wind loading and its effects on photovoltaic modules: An experimental–computational study to assess the stress on structures. *Solar Energy*, vol. 240, pp. 315–328, 2022.